Optical constants and critical point transitions in biaxially tensile-strained epitaxial germanium thin films

Rutwik Joshi[1], Nina Hong[2], Neha Singh[2], Muntasir Mahdi[1], and Mantu K. Hudait[1*]

[1]*Advanced Devices & Sustainable Energy Laboratory (ADSEL), Bradley Department of Electrical and Computer Engineering, Virginia Tech, Blacksburg, Virginia 24061, USA*

[2]*J.A. Woollam Co. Inc., Lincoln, Nebraska 68508, USA*

We present the optical properties of epitaxial germanium (Ge) thin films as a function of tensile strain from 0 % to 1.96 %, measured using variable angle spectroscopic ellipsometry in the energy range of 0.5 eV to 4.1 eV. The band structure of unstrained Ge is modified using epitaxial tensile strain imparted by the underlying compositionally controlled $In_xGa_{1-x}As$ strain template. The degeneracy of Ge's light hole (LH) and heavy hole (HH) bands near the Γ-point is lifted due to tensile strain while the Γ and L valleys descend. Such changes in the band structure impact the optical properties of tensile strained Ge such as the dielectric constant, refractive index, and absorption coefficient. At the Γ-point, it is noticed that the absorption coefficient gradually increases with tensile strain, indicating a shift in the effective band edge of Ge. Further, it is observed that the indirect transitions are dominated by L-LH, whereas the direct transitions are contributed from the Γ-LH as well as the Γ-HH due to the interplay between the transition energy and joint density of states. In addition, the tensile strain is seen to affect the band structure at different regions in the Brillouin zone (BZ) resulting in the movement of the critical points (CPs) to lower energy in the optical spectrum. The E_1 and $E_1 + \Delta_1$ CPs in tensile strained Ge are red-shifted compared with unstrained Ge. The observed movement of the E_1, and E_0 CP peaks is in close agreement with the first principles calculated band structure. Further, the apparent value of the E_0 spin-orbit (SO) energy, Δ_0 is seen to decrease with increasing tensile strain at the Γ-point. Interestingly, the E_1 SO energy, Δ_1 at the Λ-direction in the BZ remains constant indicating a very low shear deformation-related shift in the band structure due to biaxial tensile strain. As tensile-strained Ge thin films have a wide range of potential applications in electronics, sensing, and photonics, further understanding of tensile strain in Ge and its impact on its dielectric and optical properties is essential.

Keywords: *Germanium optoelectronics, tensile strained Ge, Germanium, optical constants, refractive index, absorption coefficient, critical points, spin-orbit coupling, spectroscopic ellipsometry, optical characterization*

Date Received:

I. INTRODUCTION

Germanium (Ge) has been gaining popularity for applications in optoelectronics, photonics [1-3], beyond Moore electronics [4-6], and sensing [7], as well as potential applications in quantum technologies [8, 9] over recent years. One common solution for realizing Ge optoelectronics has been integration on a silicon (Si) substrate [10]. However, the growth of Ge on Si has a high lattice misfit (~ 4 %), causing defects and dislocations, hindering optoelectronic functionality through reduced minority carrier lifetime [11,12], and defect-induced shot noise [13]. Furthermore, a coherent light source (an integral component of many on-chip optoelectronic technologies) can be realized monolithically using Ge [10], GeSn [14,15], GeSn/SiGeSn [16], or tensile strained Ge (ε-Ge) [1,17] gain media on a Si or GaAs substrate. Additionally, the heterogeneous integration of different monolithic chiplets to form diverse functionalities is an essential step toward scalable quantum technologies [18]. Using monolithically grown Ge-on-InGaAs quantum well (QW) laser chiplet, one may potentially reduce the complexity and cost of the process and enable on-chip optoelectronics. This GaAs-based monolithic configuration (*i.e.*, $In_xGa_{1-x}As$ and $In_xAl_{1-x}As$ buffers on a GaAs substrate) is a solution for growing crystalline Ge (apart from the well-controlled tensile strain) for two key reasons: (i) lower defect density due to lattice proximity [1], and (ii) transferability of GaAs technology to Si substrate [1,19]. For the tensile strained Ge on InGaAs (ε-Ge/InGaAs) based photonic devices, carrier, and optical confinement are indispensable for efficient operation, and it can be achieved via large band offsets [17] as well as the large differences in the refractive indices [1, 17] between the waveguide and cladding semiconductors. The band offsets as a function of strain in Ge layers grown on $In_xGa_{1-x}As$ buffers were determined using x-ray photoelectron spectroscopy, and the dependence of Ge-on-InGaAs band offsets on tensile strain was discussed in Ref. 17. The refractive index, dielectric constants, optical properties, critical points (CPs), and spin-orbit (SO) couplings as a function of strain in Ge layer was not demonstrated to date. In the past, the optical properties such as the refractive index ($n + ik$), dielectric functions ($\varepsilon_1 + i\varepsilon_2$), band structure, absorption coefficient (α), and Van-Hove singularities (critical points) of unstrained Ge have been studied as a function of growth, measurement temperature, doping, Sn composition, and different growth methods [20-25]. In addition, the impact of biaxial strain on the dielectric constants of Si epi-layers has been studied [26].

However, biaxially tensile strained Ge's optical properties, dielectric constants, and CP transitions were not investigated.

In this paper, we explore the impact of tensile strain on the dielectric constants and optical properties of Ge and ε-Ge through variable angle spectroscopic ellipsometry (VASE) as a function of tensile strain (ε) in Ge via $In_xGa_{1-x}As$ strain template underneath the Ge layer. The indium (In) composition in the $In_xGa_{1-x}As$ layer is varied between the samples to change the tensile strain imparted on Ge. This study aims to highlight the optical properties of epitaxial Ge layers and their dependence on the epitaxial biaxial tensile strain, as the tensile strain is gradually increased between the 6 samples, without creating relaxation-induced defects (*i.e.*, adhering to the critical layer thickness) and maintaining crystallinity [1, 27]. Each sample and their ***k.p*** calculated band structure [1] schematics are summarized in **Fig. 1(a)-(f)** in increasing order of tensile strain in the epitaxial Ge. The methodology for the pseudomorphic sample growth is discussed followed by the measurement setup for the VASE system. The model and its goodness of fit are evaluated, and dielectric constants are extracted. A clear shift in the band edge is seen through the absorption spectrum with increasing tensile strain along with an increase in absorption coefficient. Moreover, the direct and indirect bandgap of ε-Ge determined from this study is in good agreement with the 30×30 ***k.p*** calculated results [1]. The Van-Hove singularities in the band structure of ε-Ge are discussed and a gradual decrease in the E_0, $E_0 + \Delta_0$, E_1, $E_1 + \Delta_1$, and E_0' CPs is seen. Interestingly, it is observed that the SO coupling energy at the Γ-point Δ_0 has a decreasing trend with tensile strain. Whereas the SO coupling energy, Δ_1 in the Λ-direction associated with the E_1 peak remains nearly constant with applied tensile strain. By elucidating the biaxial tensile strain dependence on the dielectric constants of epitaxial thin film Ge, this study opens up an opportunity to improve the design process and analysis of various optoelectronic devices such as ε-Ge QW lasers [1, 4, 28], hole-centric spin qubit [29], FinFETs and MOSFETs [4], lattice-matched and unstrained Ge-based nanosheet-FETs [5], photodetectors [30], and photovoltaics [31].

II. METHODS

A. Material system: Growth and structure

III-V compound semiconductor templates such as InAlAs and InGaAs that leverage metamorphic and pseudomorphic growth are of interest as they can be used to produce high-quality tunable epitaxial layers for applications in monolithic optoelectronics [1]. As a part of this study, unintentionally (*uid*) doped epitaxial Ge thin films are grown on semi-insulating GaAs (001) substrates. Pseudomorphic ε-$Ge/In_xGa_{1-x}As$ structures were realized using a vacuum inter-connected dual chamber solid source molecular beam epitaxy (MBE) system [1, 19, 32]. An isolation between the III-V and the group IV chambers is employed to eliminate atomic interdiffusion at the Ge/InGaAs interface providing an abrupt transition from InGaAs to Ge. The desired In composition in the $In_xGa_{1-x}As$ strain template was realized using a linearly graded buffer (LGB) grown on a GaAs substrate. This growth process enables a virtually defect-free $In_xGa_{1-x}As$ metamorphic strain template, by restricting defects within the underlying strain-relaxed LGB. In addition, the virtually defect-free pseudomorphic growth of ε-Ge on $In_xGa_{1-x}As$ is possible if the thickness of the ε-Ge layer is maintained lower than the critical thickness of Ge [1, 27]. **Fig. 1** and **Table I** summarize the various ε-$Ge/In_xGa_{1-x}As$ structures grown using this MBE system and analyzed to determine the optical properties of ε-Ge as a function of tensile strain. Direct bandgaps of ε-Ge with varying tensile strain shown in Table I are calculated using the 30×30 ***k.p*** method [1], and a schematic representation of the relative movement of the band energies of the 4-bands at the Γ-point light hole (LH), heavy hole (HH), L and Γ is shown in **Fig. 1**. As the thickness of the ε-Ge layer is designed to be thinner than the critical layer thickness, the strain is not relaxed and hence the lattice misfit is translated to biaxial tensile strain. Thus, to our knowledge, this is the first report of the optical properties of ε-Ge as a function of moderate to large biaxial tensile strain in Ge. Interface abruptness is a critical attribute of determining the quality of the ε-$Ge/In_xGa_{1-x}As$ heterointerface and a 6 Å heterointerface abruptness was demonstrated for a ε-$Ge/In_{0.24}Ga_{0.76}As$ structure [32] by atom probe tomography using this MBE system and similar growth recipes calibrated using x-ray and transmission electron microscopy analysis [1, 32-34].

Semi-insulating (100) GaAs wafers that are 2° offcut towards [110] directions were used for this work. Native oxides from the surface of GaAs wafers were desorbed under the presence of arsenic (As_2) overpressure of ~10^{-5} torr at 750°C inside the III-V MBE chamber. *In-situ* reflection high-energy electron diffraction was used to monitor surface reconstruction and all stages of the growth of GaAs and InGaAs layers. After the 0.25 um GaAs layer growth at 650°C, the growth temperature was reduced to 550°C for linearly graded InGaAs buffer and constant composition InGaAs strain template. In each InGaAs graded buffer, inverse grading was incorporated which facilitated the efficient strain relaxation process [35]. Following the InGaAs buffer growth, each sample was cooled down below 175°C and then vacuum transferred to the group-IV growth chamber for Ge epitaxy. A growth temperature of 400°C (thermocouple temperature) and a growth rate of ~0.07 Å/s, were maintained throughout the Ge layer growth. More details of the growth procedure and material analysis for this MBE-grown tensile strain Ge on the InGaAs system can be found elsewhere [1, 17, 32-34].

B. VASE measurement methodology

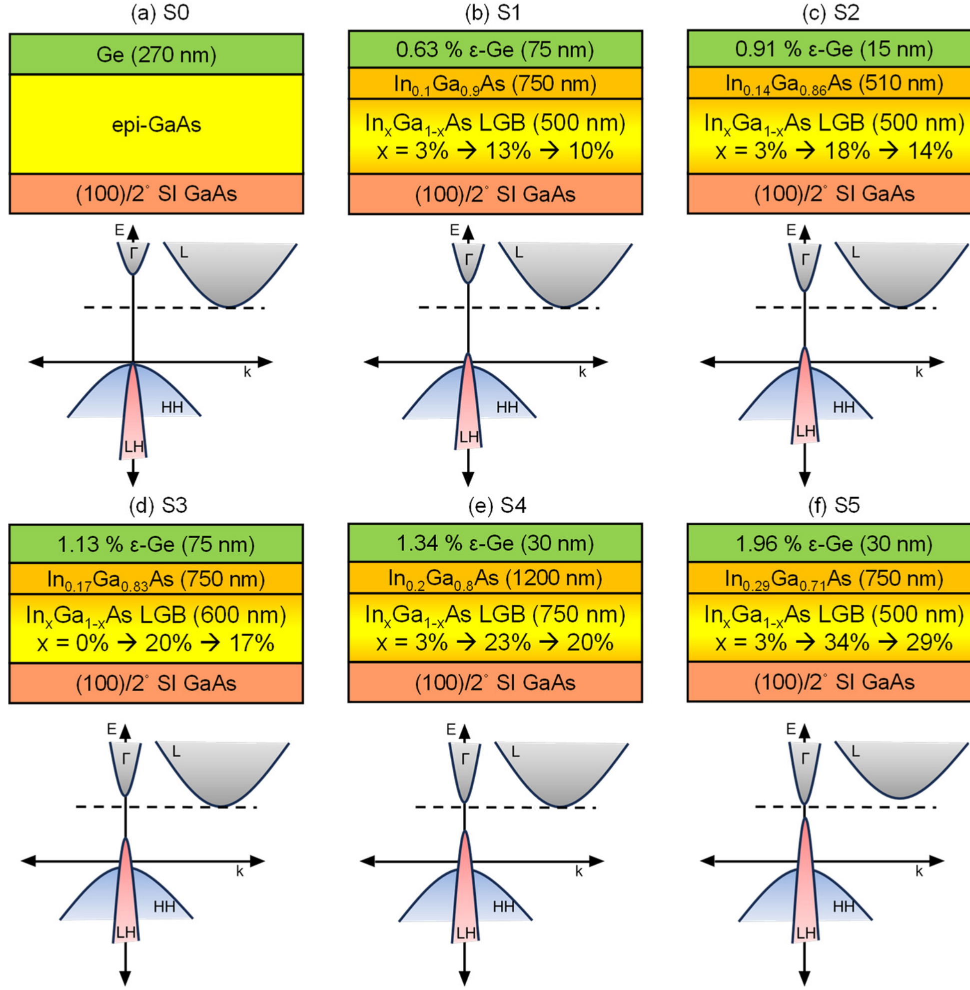

Fig. 1. Epitaxial Ge-on-InGaAs structures are grown using MBE and used in this study for optical characterization using VASE. The structures and their corresponding band diagrams are shown in the increasing order of tensile strain (a)-(f) corresponding to S0-S5 from Table I. The tensile strain is achieved using an InGaAs composition-controlled strain template grown on top of a precisely designed linearly graded buffer. These structures also represent the multilayer model used for modeling the VASE data to extract the optical constants.

Table I: Summary of ε-Ge samples used in this study as a function of In composition. The corresponding changes in the linearly graded buffer (LGB) and the direct bandgap of Ge are highlighted.

Sample Name	In composition (%) in InGaAs strain template	Thickness (nm)			Strain (%) in Ge	$E_{g,\Gamma\text{-}LH}$ (eV) | λ_g (nm)
		ε-Ge	InGaAs strain template	InGaAs LGB		
S0	0	270	0	0	-0.08	0.79 | 1570
S1	10	75	750	500	0.63	0.675 | 1837
S2	14	15	510	500	0.91	0.607 | 2042
S3	17	75	750	600	1.129	0.593 | 2091
S4	20	30	1200*	750	1.339	0.55 | 2254
S5	29	30	750	500	1.962	0.42 | 2915

Samples with varying In composition (S0-S5, *see* **Fig. 1**) were mounted each onto the vertical stage of the J. A. Woollam variable-angle-of-incidence ellipsometer system [36]. The collection of data was performed for all the samples in the range of 0.5 eV to 4.1 eV at room temperature and on the same day to avoid discrepancies due to changes in ambient and equipment configuration. The data was acquired over 4 angles of incidence for all the samples namely 60°, 65°, 70°, and 75° chosen to be around the approximate Brewster's angle for Ge. A broadband Xenon

lamp served as the light source, followed by a monochromator for wavelength selection. The incident light was polarized, and its polarization state was altered upon reflection from the sample surface. The reflected polarization was analyzed using a rotating analyzer and detected by a thermoelectrically cooled silicon/strained InGaAs stack photodiode detector. This process determined the ellipsometric angles ψ (amplitude ratio) and Δ (phase difference). The VASE measurement yielded ψ and Δ values with error bars of approximately ± 0.02° and ± 0.06°, respectively, for each sample studied here. These two quantities, ψ, and Δ, are related to the p- and s-polarization intensities through the relation [36, 37]:

$$\rho = \frac{R_p}{R_s} = \tan(\psi)\ e^{i\Delta}, \qquad (1)$$

where, ρ is the reflection coefficient ratio, R_p and R_s are the Fresnel Reflection coefficients [36, 37]. The p-polarization is defined parallel to the incident plane and the s-polarization is perpendicular, thus forming an orthogonal coordinate system. For a single-layer structure like a smooth surface bulk substrate, ψ and Δ values can be directly converted to extract the refractive index (n) and extinction coefficient (k). However, for the multilayer structures studied here (*see* **Fig. 1**), direct extraction of the optical constants from raw data is not feasible. This is because ψ and Δ are coupled indicators of the optical properties of all the layers, including the surface conditions. An iterative process is necessary to decouple the contributions of each layer in the stack (*see*, **Fig 1**) and determine their corresponding wavelength-dependent dielectric constants and thicknesses.

III. RESULTS

A. Modeling the optical spectrum of the multilayer stack to invert ψ, Δ

The objective of forming an accurate model is to decouple and extract the optical properties of Ge (n, k, ε_1, ε_2, and α) as a function of tensile strain from the measured values of ψ and Δ. The optical constants of InAs, GaAs, and $In_xGa_{1-x}As$ are known as a function of wavelength and are available with the proprietary software suite with the VASE equipment [36]. The individual layer thicknesses and compositions of all the layers in the stack are known through precisely controlled MBE growth recipes calibrated with TEM and x-ray diffraction measurements [1, 32-34] over the years. Due to the correlated nature of the optical constants and layer thicknesses, the thicknesses are held nearly constant around their nominal values during the regression analysis. This ensured that each best-fit thickness remained close to the global minimum of the mean squared error (MSE). The surface roughness and native oxide were effectively modeled as a single surface layer with its thickness as a free parameter. The index of this thin layer was approximated using the effective medium approximation (EMA) to mix the indices of the Ge film and air in a 50:50 ratio [36, 37]. This EMA layer is present above the Ge epitaxial layer in the model and is not shown in the schematic illustration in **Fig. 1**. Furthermore, the LGB shown in **Fig. 1** is subdivided into 2 sections representing the In composition gradient in $In_xGa_{1-x}As$ and the overshoot In composition. The composition-dependent optical constants of $In_xGa_{1-x}As$ were modeled using a pre-determined composition file that significantly minimized the number of fitting parameters. The thicknesses of the LGB sub-sections far away from the top surface are left as free parameters to account for unknown deviations in the optical properties of the LGB due to a high density of mismatch-induced defects. In all cases, this assumption resulted in a low mean square error (MSE) by accurately fitting the complex interference oscillations in the ellipsometry data, which arise from the complex multilayer structure beneath the Ge film.

The optical constants for the epitaxial Ge layer were modeled using a Kramers-Kronig consistent General Oscillator (GenOsc) model. The GenOsc layer incorporates multiple parametric *Psemi* oscillators [38] corresponding to various regions of electronic transitions within the band structure measured in the spectra range of 0.5 eV to 4.1 eV. The best-fit result closely matched the optical constants of the reference Ge material [21, 22, 24], *i.e.*, ($\varepsilon_1 + i\varepsilon_2$). The optical constants (n and k) of the ε-Ge films were determined through a three-step fitting process to mitigate parameter correlations. First, the film thickness and refractive index were uniquely defined using a Cauchy function in the

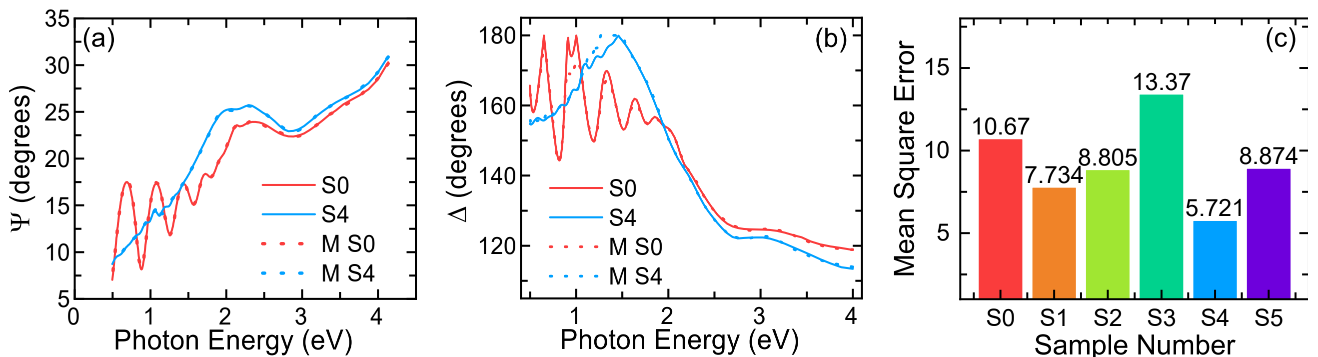

Fig. 2. Evaluating the goodness of fit of the model: Measured VASE data (solid lines: S0 and S4) and model fit (dotted lines: M S0 and M S4) for the extracted (a) ψ, and (b) Δ. (c) The corresponding mismatch between the model and measurement calculated as the MSE (unitless) indicating a good overall fit for all the samples.

transparent region. Then, with the thickness fixed, the entire wavelength range was fitted to extract both n and k using a point-by-point fit approach [38]. This extended the analysis into the absorbing region (above the bandgap energy). The point-by-point fit provided a good initial estimate, although it didn't strictly enforce Kramers-Kronig's consistency. Finally, a Kramers-Kronig consistent GenOsc model, employing parametric *Psemi* oscillators, was used to refine the optical constants. These oscillators were optimized to match the point-by-point fit results and then minimize the MSE (unitless) between the model and the measured spectroscopic data (ψ and Δ). This approach effectively captured the sharp features of the optical constants near the CPs and bandgap energy of the crystalline films. The methodology to calculate the model error through the MSE, combining relative errors in ψ and Δ, is discussed in Ref. 36. For illustrative purposes, the measured data ψ and Δ, along with the modeled values as a function of photon energy for low and high tensile strained Ge samples are shown in **Fig. 2(a) and (b)**, respectively, for one representative angle 70°. A similar method was implemented for all other tensile Ge samples. One can find that there is an excellent agreement between the measured data and the multilayer model for all 6 samples, as evidenced by the low MSE, shown in **Fig. 2(c)**.

B. Optical constants of ε-Ge

After inverting the ψ and Δ values for the multilayer stack measured and modeled at different angles for the samples over the entire spectrum, the dielectric constants ε_1 and ε_2 are extracted and shown in **Figs. 3(a,c) and (b,d)**, respectively. A clear effect of the tensile strain can be seen on both ε_1 and ε_2 indicating that there is a shift, split and/or modulation of the band structure resulting in a change in the CPs. The refractive index, n and the extinction coefficient, k are shown in **Fig. 4** as a function of photon energy as well as the corresponding wavelength. The peak value of n in this energy range can be associated with the critical point $E_1 \sim 2$ eV, which decreases with applied tensile strain while moving from a single peak for unstrained Ge to a double peak for highly tensile strained Ge. These two peaks are associated with the E_1 and $E_1 + \Delta_1$ CPs and can also be seen in **Fig. 3** in the form of peaks in the dielectric constants ε_1 and ε_2. Increasing the tensile strain results in a reduction in the refractive index at E_1 and $E_1 + \Delta_1$ peaks as well as the movement of the peaks to lower energies. The two peaks become more apparent through the split as tensile strain is applied, indicating that the broadening of the peaks is reducing due to biaxial tensile strain. To decode the impact on the CPs, second-order derivatives are extracted and presented below in the following sections. A detailed

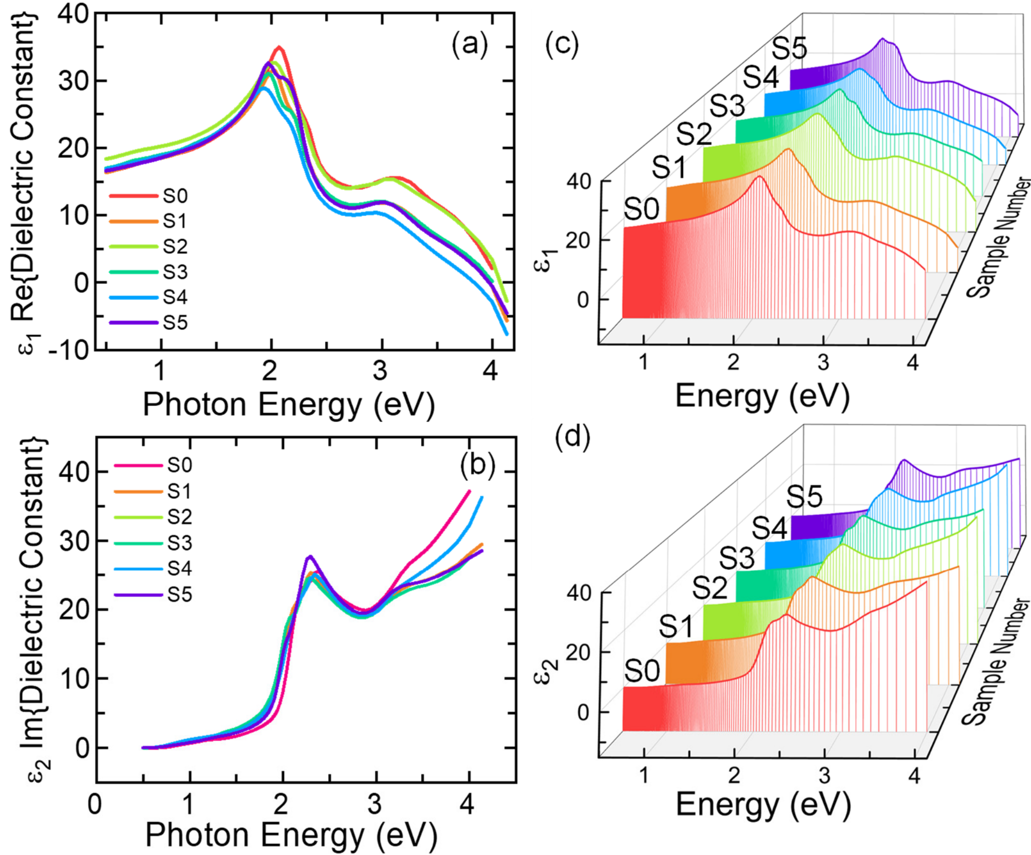

Fig. 3. The extracted dielectric constants from the ellipsometric analysis, (a) ε_1 (real part of dielectric constant) and (b) ε_2 (imaginary part of dielectric constant) as a function of photon energy. A 3D contour to visualize the movement of the various CP-related peaks in the dielectric spectrum (c) ε_1 and

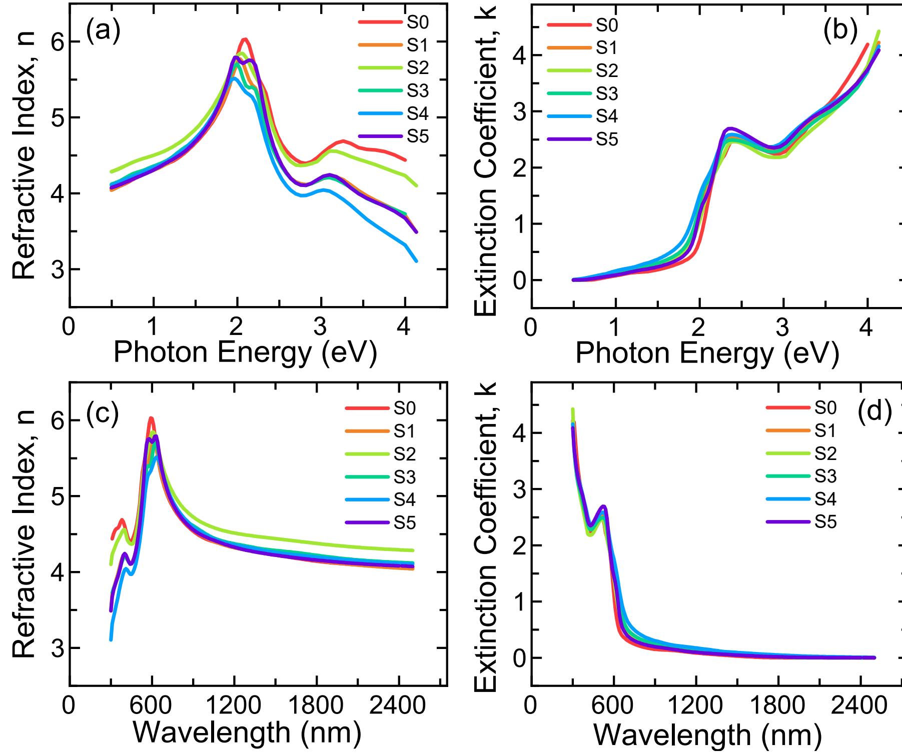

Fig. 4. A plot of (a) refractive index n and (b) extinction coefficient k as a function of photon energy for the samples S0-S5 indicating the impact of increasing tensile strain on the optical constants. The optical constants and the impact of tensile strain on a wavelength scale for (c) n and (d) k.

theoretical analysis of the CP trends due to tensile strain in Ge is also presented.

In the UV region near 3 eV increasing tensile strain results in a reducing refractive index. The refractive index near the band edge associated with the near-infrared (NIR) region is a cumulative function of the local joint density of states (JDOS), and transitions between direct valleys LH, heavy hole (HH), and Γ as well as the indirect valley L all of which are affected by the tensile strain. Similar trends can be seen for the extinction coefficient k shown in **Fig. 4**. Using the optical spectrum determined for ε-Ge, certain interesting trends for the refractive index can be defined in the three regions of particular interest based on the application space, *i.e.*, i) 400 nm UV for photonic and quantum applications, ii) 2 eV region where the E_1 CP peak refractive index lies, and iii) at the band edge of ε-Ge for NIR optoelectronics such as Ge QW lasers. The refractive index in these 3 regions is summarized in **Fig. 5(a)** for the 400nm region, **Fig. 5(b)** for the maximum refractive index region near the E_1 CP, and **Fig. 5(c)** at the respective ***k.p*** bandgaps of the samples. Estimated best-fit trend lines are displayed. In the UV region at 400 nm (**Fig. 5a**), the average reduction in the refractive index per unit percentage tensile strain is $\Delta n/\Delta\varepsilon \sim 0.5/2$. At the E_1 CP (**Fig. 5b**), the average reduction in the refractive index per unit percentage of tensile strain is $\Delta n/\Delta\varepsilon \sim 0.5/2$. Whereas, the average reduction in the refractive index at the respective bandgaps of the tensile strained samples is ~ 0.1/2 (**Fig. 5c**). As seen in **Fig. 5(b)**, the refractive index n of Sample S5 at the E_1 CP is seen to have a smaller reduction

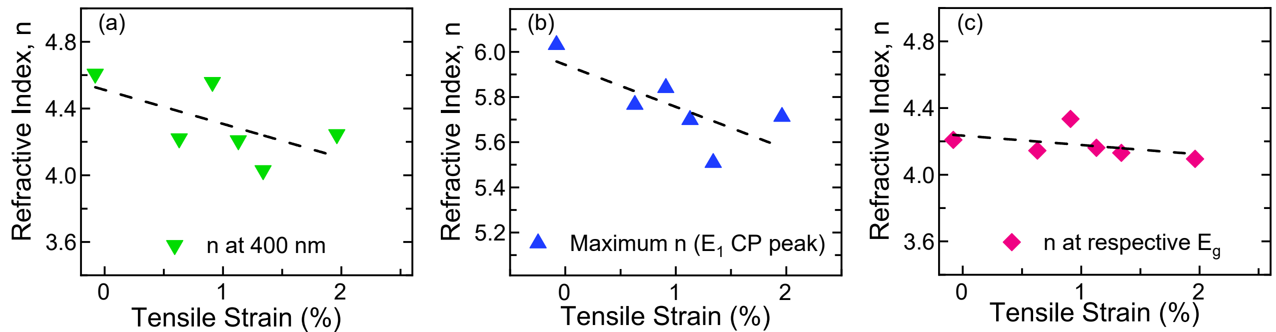

Fig. 5. Specific refractive index values as a function of tensile strain, (a) at 400 nm UV region, (b) maximum possible value at the E_1 CP peak, and (c) exactly at the respective ***k.p*** bandgaps of each sample S0-S5.

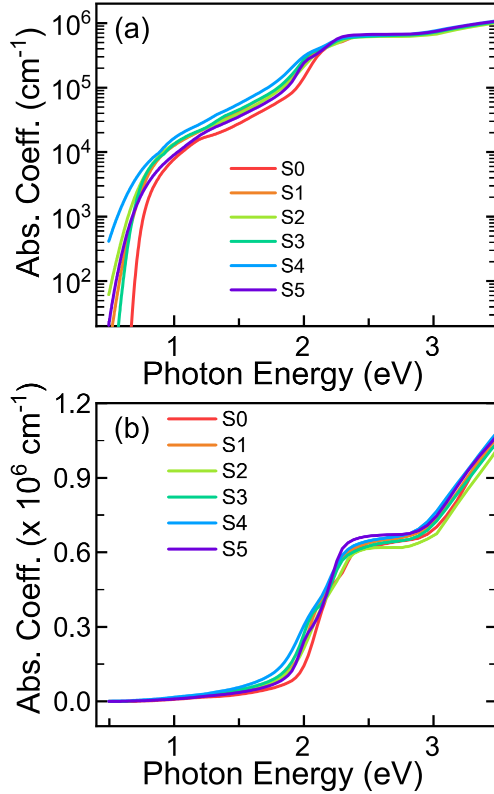

Fig. 6. The absorption coefficient determined for the samples S0-S5 indicating a shift in the absorption spectra due to the tensile strain, (a) log scale and (b) linear scale.

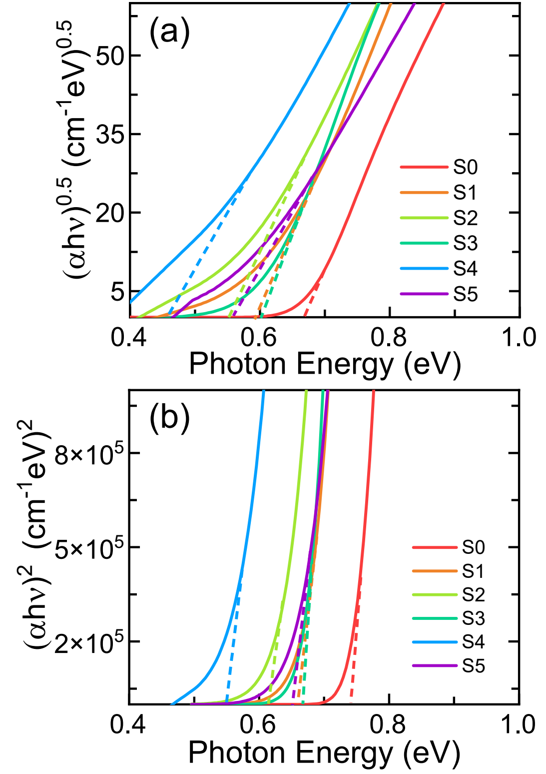

Fig. 7. Using the Tauc's method to extract the approximate (a) indirect and (b) direct band edges for the samples as a function of tensile strain. The fitting while ensuring $R^2 \sim 0.99$ for all samples is overlaid on the curves. Due to the highly linear nature and R^2 often approaching 0.999, the error in the energy intercept is < 1meV.

than expected with respect to the trend line, potentially being an outlier. The exact cause of this behavior for S5 is unclear at the time of this study. Thus, the optical properties of Ge can be tuned using epitaxial tensile strain during growth via In composition-controlled InGaAs strain template.

C. Absorption coefficient of ε-Ge

The knowledge of the absorption spectrum for epitaxial Ge and ε-Ge can assist in designing and optimizing new light sources such as lasers, LEDs, photodetectors, and optical components. The absorption coefficient for the samples S0-S5 in log and linear scale is shown in **Fig. 6(a) and (b)**, respectively. The absorption coefficient in the MIR region increases with increasing tensile strain for all the samples, with S5 seeing a smaller increment than expected. As the tensile strain is increased, a general shift in the absorption edge to lower energies is seen in **Fig. 6** near the band edge at the MIR region. This change in absorption edge can be quantified by calculating the band gap in the following section.

D. Determination of the direct and indirect bandgaps ε-Ge

Using Tauc's method, the absorption coefficient can be analyzed to determine the direct and indirect band edges in Ge and ε-Ge, further enabling analysis of the spectrum seen in **Fig. 6**. This can be done by fitting the linear plot of the absorption coefficient *versus* the photon energy [39, 40]. However, this method comes with a degree of approximations and fitting-induced uncertainty [41]. The fitting is done while maximizing the R^2 fitting values for all samples and following an identical fitting process in the region where the absorption coefficient is 10^3-10^4 cm^{-1} or higher [40]. **Fig. 7** shows the raw fitting for the indirect band edge as well as the direct band edge extraction for visualizing Tauc's method for ε-Ge samples. It is evident from **Fig. 7(a)** that the indirect band edge lies in the vicinity of ~ 0.66 eV as expected at room temperature and moves to lower energies as tensile strain is applied. Similarly, the direct band edge in **Fig. 7(b)** lies in the vicinity of ~ 0.78 eV and moves to lower energies as tensile strain causes deformation of the bands.

Interestingly, it is possible to note a few consequential observations from comparing these band edges with the band movement known through theoretical 30×30 ***k.p*** calculations for ε-Ge [1]. **Fig. 8** highlights the various direct and indirect band edges as a function of tensile strain as well as the possible transitions in the band structure that could

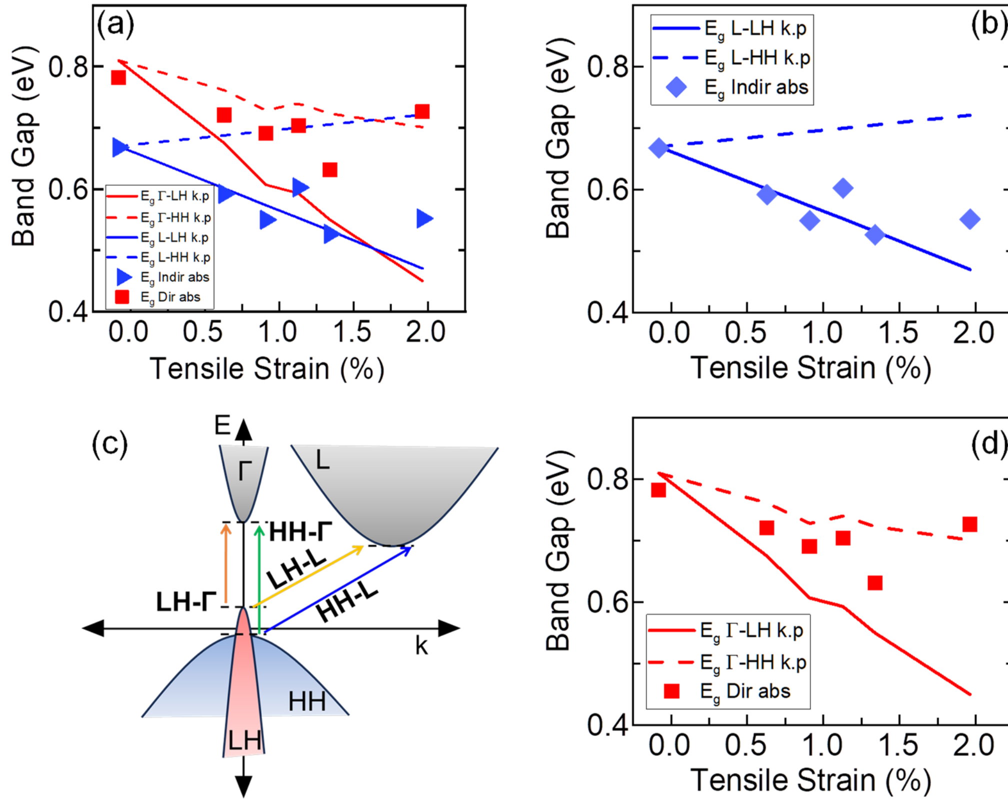

Fig. 8. (a) The approximate direct and indirect bandgaps for the 6 samples S0-S5 as a function of tensile strain compared with the relative band edge shifts calculated to 30×30 ***k.p***. (b) The indirect bandgap for the 6 samples indicating that the L-LH valley transition is dominant over the L-HH. (c) The 4 dominant transitions in this energy range are highlighted using a schematic. (d) the direct bandgaps measured for the 6 samples indicating a contribution from both Γ-HH and Γ-LH transitions with a mid-way trend. Here the solid data points are from VASE measurements.

potentially cause them. Due to the broken degeneracy between the LH and HH bands, transitions are possible from both. Compared with ***k.p*** calculated band edge movement (*see* **Fig. 8b**), it appears that indirect transitions prefer the L-LH transition over the L-HH as the latter one has an increasing transition energy. One possible explanation for this observed behavior could be the relative impact of JDOS and the transition energy (E_{tr}). Both these transitions have a large JDOS due to the large DOS of the L valley, so the differentiating factor becomes the transition energy E_{tr}. The transition rate depends linearly on the JDOS, but the dependence on the E_{tr} is exponential. Thus, although the L-HH transition will have a larger JDOS compared to L-LH, the difference is not sufficient to compensate for the exponential dependence on E_{tr}.

For the direct transitions associated with the Γ-valley and the LH or HH bands (*see* **Fig. 8c**), the E_{tr} and the JDOS will impact the relative strength of each transition. It is clear from **Fig. 8(d)** that the transitions take place from both potential paths, Γ-LH and Γ-HH as the solid data points (measured using VASE with Tauc's method) lie between the two predicted band edges for these transitions. Transitions from the LH band are insignificant for the unstrained sample, as the JDOS is very low and the E_{tr} is the same as the HH transition. For the unstrained Ge sample, it is not possible to determine the origin of transitions (LH or HH) as the bands are degenerate. However, the transition rate for the Γ-HH transitions will have a much larger JDOS, hence it can be expected that the transitions are primarily originating from the Γ-HH transition coupling. As tensile strain is applied, the degeneracy is broken, and the LH transitions become exponentially more probable than HH transitions. Thus, the observed direct band edges lie somewhere in between the two possible transitions as seen in **Fig. 8(d)**.

E. Van-Hove singularities in Ge as a function of tensile strain

The absorption of light can be described as a direct electronic transition between two energy states in the band structure or a transition assisted by the excitation of a phonon. Transitions following momentum conservation (selection rules) are more probable where the joint electronic density of states shows a CP associated with a delta function $\delta\,(h\nu - E_{cp})$ in the JDOS. These inter-band transitions can be characterized using the numerical second-order derivative (*see* **Fig. 9**) of the complex dielectric function versus the

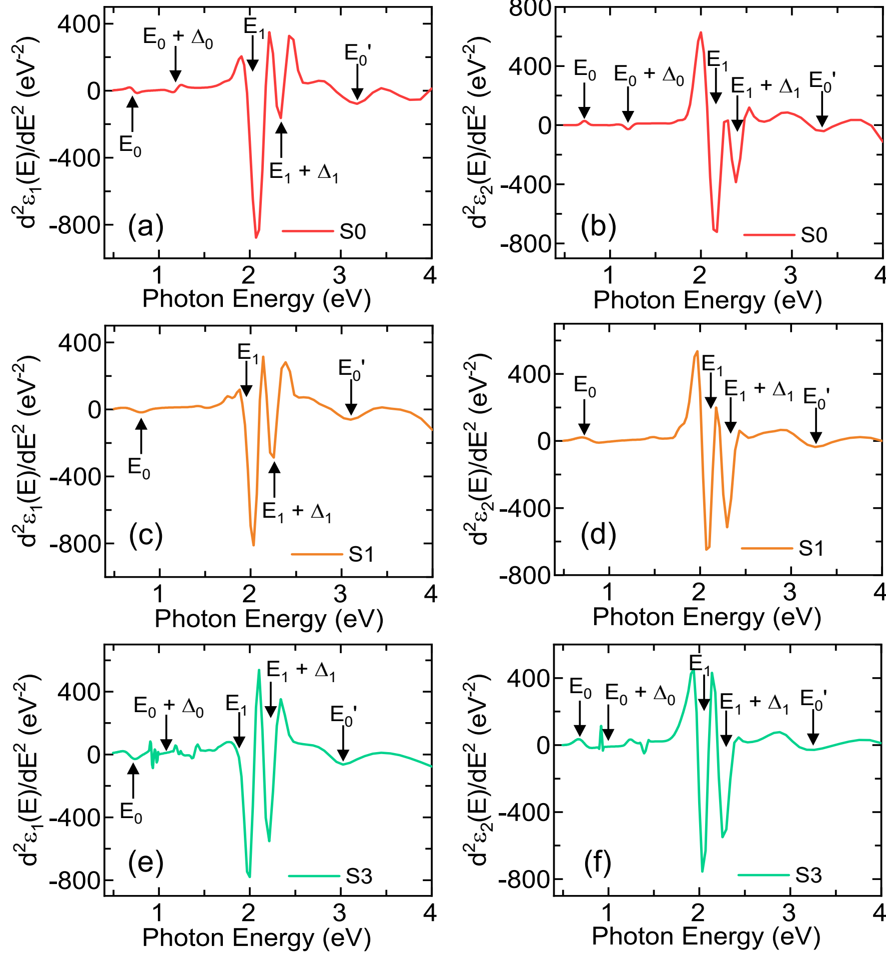

Fig. 9. Van Hove singularities: the critical points have been shown for unstrained, moderately strained and highly strained samples using the second derivative of the dielectric functions. The extracted CP energies are shown for the 5 CPs visible in this range of the spectrum.

photon energy (*see* **Fig. 3**). The dielectric constant ($\varepsilon_1 + i\,\varepsilon_2$) as a function of the photon energy of Ge has a few specific inflection points in this energy range (0.5 eV to 4.1 eV) which can be enhanced using the second order derivative and linked to specific direct band transitions between various regions of the Brillouin zone. Such transitions have a fixed energy difference between the valence band (VB) and conduction band (CB), across many high-symmetry directions in the crystal structure of Ge and may not always relate to transitions between just a single pair of bands. This CP structure and the locations of various CPs in the band structure of Ge and *ε*-Ge is shown in **Fig. 9** for 3 samples to illustrate the ability of the 2nd order derivative of the dielectric functions to enhance the CPs. The numerical second-order derivative is calculated using the Stravitzky-Golay algorithm with a 5th-order polynomial interpolation between adjacent data points and a 10-point calculation window, stitched together to form the derivative spectra for the entire photon energy range.

Some general observations can be drawn from the trends seen in **Fig. 9**: i) E_0 and $E_0 + \Delta_0$ CPs have a smaller transition amplitude compared to the others, ii) E_1 and $E_1 + \Delta_1$ CPs have the largest amplitude and the smallest broadening, iii) $E_0{}'$ CP is the broadest with a large broadening factor, and iv) tensile strain moves all these CPs to lower energies. The CPs are extracted by fitting the derivative spectrum of the dielectric functions ε_1 and ε_2 (*see* **Fig. 3**) simultaneously to the derivative of the complex Lorentzian [24, 25]. The fitting function has 4 parameters (E_{tr}, φ, Γ_{Ei}, and A) which are fit using a Levenberg–Marquardt algorithm for least square regression, ensuring an R^2 value tending to 1. The parameter E_{tr} is associated with the CP energy peak and is central to this study, φ, Γ_{Ei} and A are the phase, broadening factor, and amplitude of the CP, respectively. The complex Lorentzian function is fitted to the derivative of the dielectric function near the E_0 and $E_0 + \Delta_0$ CP such that [25],

$$\frac{d^2\varepsilon}{dE^2} = \frac{A_{E0}\, e^{i\varphi}}{(E - E_0 + i\Gamma_{E0})^{3/2}} \;. \quad (2)$$

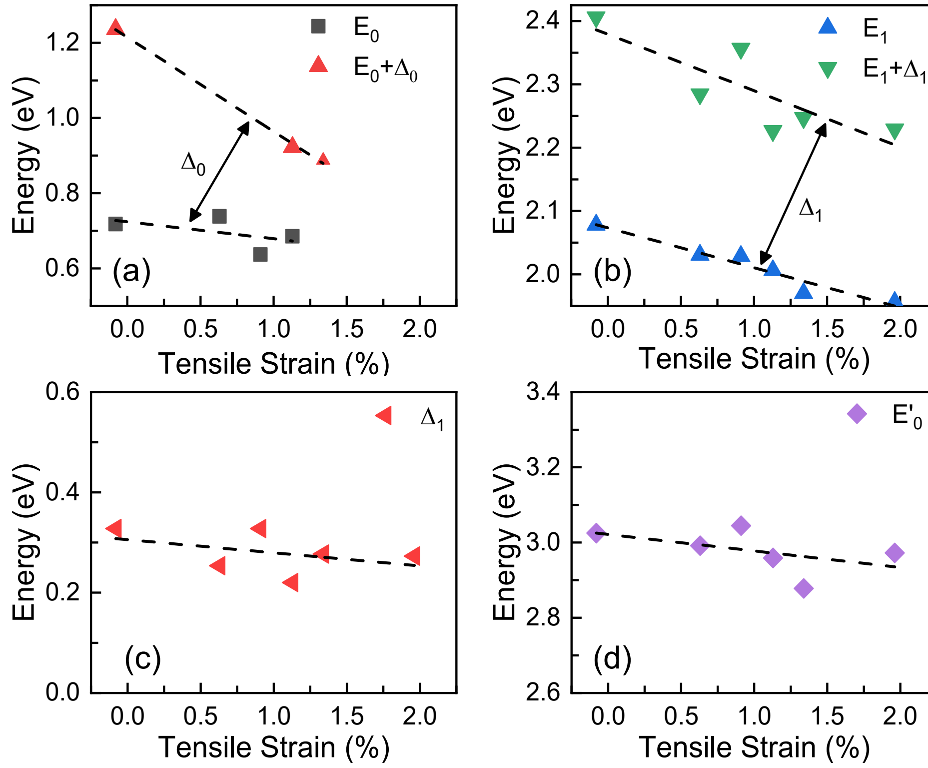

Fig. 10. CP values as a function of strain in Ge layers. (a) The CP associated with the (a) fundamental band edge at E_0 and SO coupling E_0+ Δ_0, (b) the E_1 and $E_1 + \Delta_1$ CP at the Λ-axis, (c) the SO energy Δ_1 obtained from the difference in the E_1 and $E_1 + \Delta_1$ CP, and (d) the E_0' CP remaining nearly constant with applied tensile strain. The error in the CP energy peak after the fitting is of the order of ~ 2 meV for the E_0 peak, ~ 8 meV for the E_1 peak, and 25 meV for the E_0' peak.

Here, $\varepsilon = \varepsilon_1 + i\,\varepsilon_2$ is the complex dielectric constant. Similarly, the E_1 and $E_1 + \Delta_1$ CPs are fit simultaneously with the same expression for the two transitions. An additional fitting parameter Δ_1 (not to be confused with the Δ used to represent the measured ellipsometric angle in the earlier section) is introduced in the fitting process to represent the spin-orbit coupling energy in the Λ-direction. The E_1 and $E_1 + \Delta_1$ CP transitions are modeled using [25],

$$\frac{d^2\varepsilon}{dE^2} = \frac{A_{E1}\, e^{i\varphi}}{(E - E_1 + i\Gamma_{E1})^2}, \quad (3)$$

$$\frac{d^2\varepsilon}{dE^2} = \frac{A_{E_1+\Delta}\, e^{i\varphi}}{(E - E_1 - \Delta + i\Gamma_{E_1+\Delta})^2} \quad .(4)$$

The extracted CP energies as a function of tensile strain using the fitting process shown in Eqs. 2, 3, 4 and second-order derivates in **Fig. 9** are summarized in **Fig. 10(a)-(d)** for the 5 CPs. The CP associated with the direct gap E_0 is at the center of the Brillouin zone at the Γ-point, as a 3-dimensional minima M_0. The CP near E_0 has the form $(E - E_0)^{0.5}$ in the absence of excitonic effects as is expected at room temperature. The E_0 transition is observed near the 0.5 eV - 0.8 eV spectral region and is directly linked to the fundamental band edge of Ge usually reported in the literature occurring between $\Gamma_{25'}$ - $\Gamma_{2'}$ regions of the Brillouin zone. The CP E_0 determines most of the dielectric dispersion below the band edge since there are no other CPs below E_0. The effect of epitaxial tensile strain can be understood as a perturbation resulting in a red shift of the E_0 CP, as seen in **Fig. 10(a)**. However, such a redshift into the MIR region moves closer to the end of the measurable range of the VASE equipment, and results in poor sensitivity for this transition for Ge samples with high tensile strain. Note that the E_0 and the band edge can be as low as ~ 0.45 eV for highly tensile strained samples used in this study, based on ***k.p*** estimates. The E_0 transition is thus detectable as a weak artifact only for the moderately strained samples and the unstrained Ge sample. Similarly, the $E_0 + \Delta_0$ CP associated with the SO coupling also follows a similar decreasing trend as seen in **Fig. 10(a)**. Although the number of extractable values of the $E_0 + \Delta_0$ and E_0 CP is not large as seen in **Fig. 10(a)**, due to the end of the measurable range in our current VASE setup, however, certain observations can be made. The SO energy Δ_0, *i.e.*, the difference in the $E_0 + \Delta_0$ and E_0 CP energies, is seen to decrease with applied tensile strain in Ge, indicating that this apparent value of the SO coupling reduces with tensile strain. Thus, it can be reasonable to expect that at a

certain tensile strain value beyond ~ 2.5%, the apparent SO coupling energy Δ_0 will tend to be zero or negative. Due to the broken degeneracy between the LH and HH bands by the strain, the E_0 CP should be seen as two distinct peaks, $E_0(1)$ and $E_0(2)$ associated with the transition to HH and LH, respectively. At room temperature, these CPs would be broadened and closely spaced resulting in the appearance of one single CP while being indistinguishable.

The behavior of the E_0 and $E_0 + \Delta_0$ CP with applied tensile strain can be visualized in **Fig. 11(a)** which shows the split of the three transitions, indicated by arrows. By solving the strain perturbed Hamiltonian including the hydrostatic and shear strain deformations of the CB, LH, HH, and SO bands, the changes in the three transitions can be computed up to the first-order approximation using [42],

$$\Delta(E_c - E_{LH}) = -\Delta E_H - \frac{1}{2}\Delta E_S \quad (5)$$

for the LH band $\left|\frac{3}{2}, \frac{3}{2}\right\rangle$ with ΔE_H representing the hydrostatic deformation of the band and ΔE_S representing the shear deformation. For the HH band $\left|\frac{3}{2}, \frac{1}{2}\right\rangle$, the impact of tensile strain can be expressed using,

$$\Delta(E_c - E_{HH}) = -\Delta E_H + \frac{1}{2}\Delta E_S - \frac{1}{2}\frac{(\Delta E_{S'})^2}{\Delta_0}. \quad (6)$$

Similarly, the SO band transition energy shift can be calculated using,

$$\Delta(E_c - E_{so}) = \Delta_0 - \Delta E_{H'} + \frac{1}{2}\frac{(\Delta E_{S'})^2}{\Delta_0}. \quad (7)$$

The terms ΔE_H, ΔE_S, $\Delta E_{H'}$, and $\Delta E_{S'}$ are computed using the compliance constants and Ge 300 K material parameters from Ref. [43]. The deformation potential for the hydrostatic components (C_1 + a) and (C_1 + a') are assumed to be -10.9 eV and -11.2 eV, respectively. The shear deformation potentials b and b' are assumed to be -2.86 eV and -2.44 eV, respectively [42]. The tensile strain is assumed to be positive, and the expressions are modified accordingly as shown in Eq. 5, 6, and 7.

The SO energy Δ_0 predicted in this measurement is slightly larger than reported in the literature [42]. The exact cause of this is unknown and could be a systemic shift in the measurement and fitting process, but the objective of this analysis is to highlight the impact of tensile strain on the relative CP energy trend between samples. The theoretical CP energies as a function of tensile strain are calculated using Eq. 5, 6, and 7 (*see* **Fig. 11(b)**) and are overlaid with the measured CP energies for the E_0 and $E_0 + \Delta_0$ CP seen in this work. The unstrained SO energy Δ_0 is set at the same as the value measured for the unstrained sample S0, i.e., 0.45 eV. Although it is difficult to distinguish if the E_0 CP originates from the $E_0(1)$ or $E_0(2)$ transitions, they have a general decreasing trend aligning with the theoretical predictions. Furthermore, the reducing nature of the apparent SO energy Δ_0 is clear both in the measurements and the theoretical computations. We refrain from predicting the exact values of the SO energy Δ_0 as a function of tensile strain due to the sparse nature of the extractable CP energies in our study.

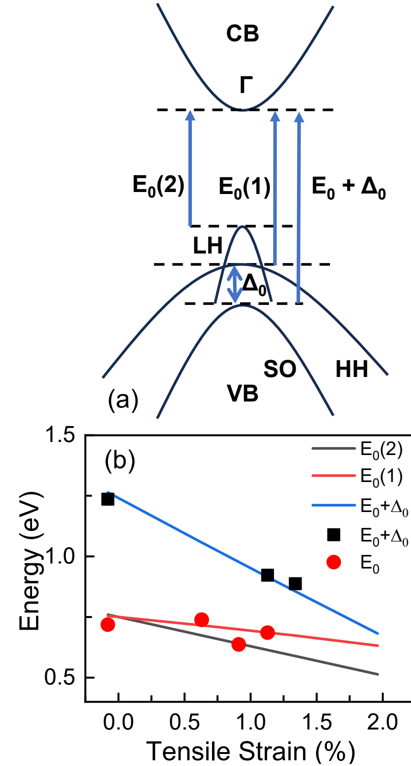

Fig. 11. Understanding the E0 CP behavior: (a) the three transitions possible after the broken degeneracy between the LH and HH bands due to the tensile strain, and (b) comparing the VASE extracted E_0 and $E_0 + \Delta_0$ CPs as a function of tensile strain, with theoretically predicted values using band theory calculations.

The artifacts associated with the E_1 and $E_1 + \Delta_1$ CPs are due to transitions between the top two VBs and the lowest CB along <111> direction in the Brillouin zone (Λ-axis). The E_1 CP is associated with the transitions between Λ_1 CB and the $\Lambda_{4,5}$ VB, whereas the $E_1 + \Delta_1$ CP is associated with the transition between the Λ_1 CB and the Λ_6 VB. Along this direction, the VB and CB are nearly parallel, represented by 2-dimensional minima in the band structure. The location and the dependence of the E_1 and $E_1 + \Delta_1$ CP energy on the tensile strain in Ge are shown in **Fig. 10(b)**. The peak energy associated with this CP decreases with increasing tensile strain in Ge. The difference in the two trends is the SO energy Δ_1, and a nearly fixed Δ_1 ~ 0.25 eV can be observed even with increasing tensile strain in Ge. The value of the

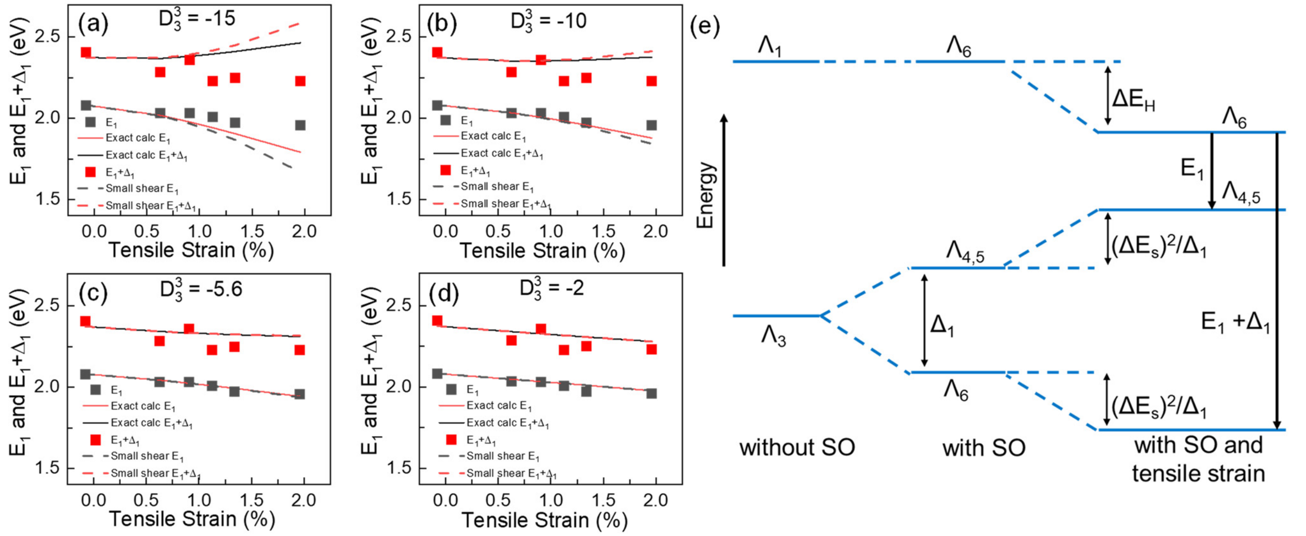

Fig. 12. Understanding the E_1 CP behavior: Impact of the choice of shear deformation potential, (a) -15, (b) -10, (c) -5.6 and (d) -2 on the theoretically predicted value compared with the extracted VASE CP values. (e) Energy bands and corresponding transitions in the low shear approximation at the Λ axis for the E_1 CP.

SO energy Δ_1 (*see* **Fig. 10c**) is slightly larger than values usually reported in the literature of ~ 0.2 eV for Ge. This shift in the apparent value of the SO energy could be due to a strain-independent term introducing a constant energy shift. The exact cause of this deviation is unknown at the time of writing this manuscript.

Further analysis of the E_1 and $E_1+\Delta_1$ peak is possible based on the red shifting trend seen in **Fig. 10(b)** to reveal some interesting mechanisms as the measured data is compared with the theoretical predictions. The impact of the SO coupling and the applied tensile strain is shown for the E_1 and $E_1+\Delta_1$ peak in **Fig. 12**. The shear and hydrostatic components of the strain have been separated, ΔE_s and ΔE_H, respectively. The hydrostatic deformation ΔE_H is calculated using [43],

$$\Delta E_H = \frac{2\,D_1^1}{\sqrt{3}}\left(1-\frac{c_{12}}{c_{11}}\right)\varepsilon_{out-of-plane}, \quad (8)$$

where c_{12} and c_{11} are the elastic constants, ε is the strain applied to the lattice and D_1^1 is the hydrostatic deformation potential for the CB at E_1. The typical values of c_{11} and c_{12} 128.5 GPa and 48.3 GPa, respectively, are used in this analysis [43]. The strain is a fractional number of the order of 0.01 and the hydrostatic deformation potential D_1^1 is -8.7 eV. The shear deformation of the VB can be calculated using [43],

$$\Delta E_s = -\sqrt{\frac{2}{3}}\,D_3^3\left(1+\frac{2c_{12}}{c_{11}}\right)\varepsilon_{out-of-plane}, \quad (9)$$

where the shear deformation potential for the E_1 VB is denoted by D_3^3 having a value of -5.6 eV. The out-of-plane strain $\varepsilon_{out-of-plane}$ can be computed by knowing the biaxial relaxation constant R_B where $\varepsilon_{out-of-plane} = -R_B\,\varepsilon_{in-plane}$. The applied tensile strain redshifts the E_1 peaks as seen in **Fig. 10(b)**. The shifts in E_1 and $E_1+\Delta_1$ peak can be theoretically computed using the following relation obtained by solving for the eigen energies of the strain Hamiltonian considering the SO coupling,

$$\partial(E_1)_t = \frac{\Delta_1}{2} - \Delta E_H - \frac{1}{2}\sqrt{{\Delta_1}^2 + 4\,(\Delta E_s)^2}\ , \quad (10)$$

$$\partial(E_1+\Delta_1)_t = -\frac{\Delta_1}{2} - \Delta E_H + \frac{1}{2}\sqrt{{\Delta_1}^2 + 4\,(\Delta E_s)^2}\,. \quad (11)$$

Here, $\partial(E_1)_t$ and $\partial(E_1+\Delta_1)_t$ indicate the difference of CP energy between the unstrained Ge and ε-Ge. The difference in the two peak energies associated with the "apparent" SO energy $(\Delta_1)_t$ can be obtained as,

$$\Delta_{1,t} = (E_1+\Delta_1)_t - (E_1)_t = \frac{1}{2}\sqrt{{\Delta_1}^2 + 4\,(\Delta E_s)^2}\,. \quad (12)$$

It is evident that the apparent SO energy $\Delta_{1,t}$ will be amplified regardless of the type of strain applied, tensile or compressive, due to the squared dependence of the shear-induced energy shift. A simplification can be made by assuming that the shear-induced energy shift is much smaller than the SO energy Δ_1, the expressions can be simplified by expanding the series to obtain,

$$\partial(E_1)_t = -\Delta E_H - \frac{(\Delta E_s)^2}{\Delta_1}, \quad (13)$$

$$\partial(E_1 + \Delta_1)_t = -\Delta E_H + \frac{(\Delta E_s)^2}{\Delta_1}. \quad (14)$$

This can further be used to obtain the simplified apparent SO energy $\Delta_{1,t}$ for tensile strained Ge,

$$\Delta_{1,t} = (E_1 + \Delta_1)_t - (E_1)_t = \Delta_1 + 2\frac{(\Delta E_s)^2}{\Delta_1}. (15)$$

The quadratic dependence of ΔE_s on the sign of the strain value, creates a shift that is independent of the type of strain, i.e., tensile or compressive.

To evaluate the validity of the exact equation described in Eq. 10, 11, 12 and the small shear approximation expressions in Eq. 13, 14, 15, the model-predicted E_1 and $E_1 + \Delta_1$ energies are overlaid with the extracted VASE data. **Fig. 12(a), (b), (c), and (d)** show the impact of different shear deformation potentials (-15 eV to -2 eV) on the band edge movement while comparing it with the VASE-extracted CP energies. The transitions discussed in Eqs. 10, 11, and 12 is schematically illustrated in **Fig. 12(e)** to show the E_1 and $E_1 + \Delta_1$ transition in the presence of SO coupling, tensile strain, and a small shear approximation. Keeping the hydrostatic deformation potential D_1^1 fixed at -8.7 eV, **Fig. 12(a), (b), (c), and (d)** vary the shear deformation potential D_3^3 between -15, -10, -5.6 and -2 eV respectively. The typically reported value of D_3^3 is -5.6 eV [43] and hence, **Fig. 12(c)** has a better match between the predicted model values and the measured E_1 CP movement, compared to **Fig. 12(a) and (b)**. A lower value of D_3^3 in **Fig. 12(d)** agrees better than -5.6 eV with the E_1 CP data. A low shear deformation potential indicates a smaller shear component to the band movement, and a close agreement can be seen between the exact equation and the small shear approximation (*see* Fig. 12c and d). It is evident that the low-shear approximation works best for the measured ε-Ge samples are presented in this work. This seems reasonable as the epitaxial strain amounts are below 2 % in this study. One can also notice that a threshold can be identified at ~ 1 % tensile strain where the shear approximation does not fit well with the data points for a large shear deformation potential D_3^3 of -10 eV or -15 eV (*see* **Fig. 12a and b**). In the presence of a small shear deformation, looking at **Eq. 12** the apparent value of the SO splitting $\Delta_{1,t}$ will have a negligible dependence on the value of ΔE_s, which is proportional to the tensile strain ε. This explains the trend seen in **Fig. 10(c)** which shows a nearly constant SO energy Δ_1 for increasing tensile strain as well as a parallel decreasing trend for the E_1 and $E_1 + \Delta_1$ peaks. The impact of the hydrostatic and shear deformation on the various bands in Ge at the E_1 CP (Λ axis) in the presence of biaxial tensile strain is pictorially summarized in **Fig. 12 (e)** for the small shear approximation. In conclusion, we note that the epitaxial tensile strain applied to Ge thin films does not cause a large shear deformation of the VBs at the E_1 CP (Λ axis), while maintaining a nearly fixed SO splitting energy Δ_1 with increasing tensile strain.

Lastly, the E_0' CP is seen as a broadened peak in **Fig. 9** and a near-independence on the applied tensile strain is seen in **Fig. 10 (d)**. The broadened nature of the E_0' CP is due to many different regions in the Brillouin zone contributing to these high-energy transitions as well as mixing with the E_0' + Δ peak. In addition, one can also evaluate the impact of tensile strain on the φ, Γ_{Ei}, and A fitting parameters. However, this is further subject to additional fitting and measurement-related deviations, which can mask any real physical interpretation.

IV. CONCLUSIONS

Through variable angle spectroscopic ellipsometric measurements of a series of tunable tensile strained Ge thin films grown on a composition-controlled InGaAs strain template, the impact of tensile strain on the optical properties and CPs transitions of Ge is presented. As the In composition in the underlying InGaAs strain template is increased, the direct Γ-valley is lowered in energy. The spectra for the optical constants such as n, k, ε_1, ε_2, and α are measured in the range of 0.5 eV– 4.1 eV, for unstrained and tensile strained Ge thin films in the range of tensile strain from 0 – 1.96 %. It is observed that the absorption coefficient, α gradually increases with tensile strain indicating a shift in the band edge of Ge. The band edges are determined for the direct and indirect transitions. It is observed that the indirect transitions are dominated by L-LH transitions whereas the direct transitions are contributed from the Γ-LH as well as the Γ-HH transitions due to the interplay between the E_{tr} and joint density of states trends. The CPs (Van-Hove singularities) are obtained from the second derivative spectra obtained through the VASE measurement of the dielectric constants, and it is seen that the CPs moved to lower energies with increasing tensile strain. Increasing tensile strain results in a reduction in refractive index at CP E_1 and $E_1 + \Delta_1$ peaks, and the movement of these peaks to lower energies. In addition, the movement of the E_1, E_0', and E_0 CP peaks is in close agreement with the first principles calculated band structure. Furthermore, the apparent value of the E_0 and SO energy Δ_0 decreases with increasing tensile strain at the Γ-point. The E_1 and SO energy Δ_1 at the Λ-direction remains constant indicating a very low shear deformation-related shift in the band structure. Therefore, this work elucidated the impact of biaxial tensile strain on the dielectric constants, optical properties and CPs determined using spectroscopic ellipsometry of epitaxial Ge thin films as a function of tensile strain.

CONFLICTS OF INTEREST

Dr. Nina Hong and Dr. Neha Singh are affiliated with J. A. Woollam Co. Inc., the manufacturer of the equipment used in this study. Their contributions were limited to scientific and technical expertise in ellipsometry and model validation. No financial, personal, or proprietary conflicts of interest influenced the research or its outcome.

ACKNOWLEDGMENTS

M. K. H. acknowledges partial support from the NSF under grant numbers ECCS-2042079, a US-Ireland Joint R&D Program, and ECCS-2430393 as well as Virginia Tech Nanofabrication facilities for assistance during materials analysis.

AUTHOR INFORMATION

Corresponding Author**:** *Tel: (540) 231-6663. E-mail: mantu@vt.edu.

REFERENCES

[1] M. K. Hudait, F. Murphy-Armando, D. Saladukha, M. B. Clavel, P. S. Goley, D. Maurya, S. Bhattacharya, T. J. Ochalski, Design, Theoretical and Experimental Investigation of Tensile-strained Germanium Quantum-well Laser Structure, *ACS Appl. Electron. Mater.* **3**, 4535- 547 (2021).

[2] C. Sun, M. T. Wade, Y. Lee, J. S. Orcutt, L. Alloatti, M. S. Georgas, A. S. Waterman, J. M. Shainline, R. R. Avizienis, S. Lin, *et al.*, Single-chip microprocessor that communicates directly using light, *Nature* **528**, 534 - 538 (2015).

[3] K. Tani, T. Okumura, K. Oda, M. Deura, and T. Ido, On-chip optical interconnection using integrated germanium light emitters and photodetectors, *Optics Express* **29**, 28021-28036 (2021).

[4] R. Joshi, S. Karthikeyan, and M. K. Hudait, Monolithically cointegrated tensile strained germanium and $In_xGa_{1-x}As$ FinFETs for tunable CMOS logic, *IEEE Trans. Electron. Dev.,* **69**, 4175-4182 (2022).

[5] R. Joshi, S. Karthikeyan, and M. K. Hudait, Germanium Nanosheet-FETs Scaled to Subnanometer Node Utilizing Monolithically Integrated Lattice Matched Ge/AlAs and Strained Ge/InGaAs, *IEEE Trans. Electron. Dev.,* **70**, 899-907 (2023).

[6] W. Rachmady, A. Agrawal, S. H. Sung, G. Dewey, S. Chouksey, B. Chu-Kung, G. Elbaz, P. Fischer, C. Y. Huang, K. Jun, *et al.*, 300mm heterogeneous 3D integration of record performance layer transfer germanium PMOS with silicon NMOS for low power high-performance logic applications, *IEEE International Electron Devices Meeting (IEDM)*, pp. 29.7.1-29.7.4 (2019).

[7] L. Høgstedt, J. S. Dam, A.-L. Sahlberg, Z. Li, M. Aldén, C. Pedersen, P. Tidemand-Lichtenberg, Low-noise mid-IR upconversion detector for improved IR-degenerate four-wave mixing gas sensing, *Optics Letters* **39**, 5321-5324 (2014).

[8] G. L. Mansell, T. G. McRae, P. A. Altin, M. J. Yap, R. L. Ward, B. J. J. Slagmolen, D. A. Shaddock, D. E. McClelland, Observation of Squeezed Light in the 2 μm Region, *Phys. Rev. Lett.* **120**, 203603 (2018).

[9] M. Mancinelli, A. Trenti, S. Piccione, G. Fontana, J. S. Dam, P. Tidemand-Lichtenberg, C. Pedersen, L. Pavesi, Mid-infrared coincidence measurements on twin photons at room temperature, *Nature Communications* **8**, 15184 (2017).

[10] R. E. Camacho-Aguilera, Y. Cai, N. Patel, J. T. Bessette, M. Romagnoli, L. C. Kimerling, J. Michel, An electrically pumped germanium laser, *Optics Express* **20**, 11316–11320 (2012).

[11] D. S. Sukhdeo, S. Gupta, K. C. Saraswat, B. R. Dutt, and D. Nam, Impact of minority carrier lifetime on the performance of strained germanium light sources, *Optics Communications* **364**, 233-237 (2016).

[12] M. K. Hudait, S. W. Johnston, M. B. Clavel, S. Bhattacharya, S. Karthikeyan, R. Joshi, High carrier lifetimes in epitaxial germanium–tin/Al (In) As heterostructures with variable tin compositions, *J. Mater. Chem. C* **10**, 10530–10540 (2022).

[13] R. O. Behunin, F. Intravaia, and P. T. Rakich, Dimensional transformation of defect-induced noise, dissipation, and nonlinearity, *Phys. Rev.* B **93**, 224110 (2016).

[14] R. Joshi, L. F. Lester, and M. K. Hudait, Lattice Matched Tunable Wavelength GeSn Quantum Well Laser Architecture: Theoretical Investigation, *IEEE Journal of Selected Topics in Quantum Electronics (*SiGeSn Infrared Photon. and Quantum Electronics) **31**, 1-12 (2025).

[15] S. Wirths, R. Geiger, N. Von Den Driesch, G. Mussler, T. Stoica, S. Mantl, Z. Ikonic, M. Luysberg, S. Chiussi, J.-M. Hartmann, *et al.*, Lasing in direct-bandgap GeSn alloy grown on Si, *Nature Photonics* **9**, 88-92 (2015).

[16] S. -W. Chang and S. L. Chuang, Theory of Optical Gain of Ge--$Si_xGe_ySn_{1-x-y}$ Quantum-Well Lasers, *IEEE J. Quantum Electron.* **43**, 249-256, (2007).

[17] R. Joshi, S. Johnston, S. Karthikeyan, L. F. Lester and M. K. Hudait, Monolithically Integrated ϵ-Ge/$In_xGa_{1-x}As$ Quantum Well Laser Design: Experimental and Theoretical Investigation, *IEEE J. Sel. Topics Quantum Electron.* (Flexible Optoelectronics) **30**,1-15, (2024).

[18] H. Mahmudlu, R. Johanning, A. Van Rees, A. Khodadad Kashi, J. P. Epping, R. Haldar, K.-J. Boller, M. Kues, Fully on-chip photonic turnkey quantum source for entangled qubit/qudit state generation, *Nature Photonics* **17**, 518–524 (2023).

[19] A. Ghosh, M. B. Clavel, P. D. Nguyen, M. A. Meeker, G. A. Khodaparast, R. J. Bodnar, M. K. Hudait, Growth, structural, and electrical properties of germanium-on-silicon heterostructure by molecular beam epitaxy, *AIP Advances* **7**, 095214 (2017).

[20] M. R. Bauer, J. Tolle, C. Bungay, A. V. G. Chizmeshya, D. J. Smith, J. Menéndez, J. Kouvetakis, Tunable band structure in diamond–cubic tin–germanium alloys grown on silicon substrates, *Solid State Communications* **127**, 355-359 (2003).

[21] T. N. Nunley, N. S. Fernando, N. Samarasingha, J. M. Moya, C. M. Nelson, A. A. Medina, S. Zollner, Optical constants of germanium and thermally grown germanium dioxide from 0.5 to 6.6 eV via a multisample ellipsometry investigation, *J. Vac. Sci. Technol. B* **34**, 061205 (2016).

[22] G. E. Jellison Jr., Optical functions of GaAs, GaP, and Ge determined by two-channel polarization modulation ellipsometry, *Optical Materials* **1**,151-160 (1992).

[23] C. Xu, C. L. Senaratne, J. Kouvetakis, and J. Menéndez, Compositional dependence of optical interband transition energies in GeSn and GeSiSn alloys, *Solid State Electron.* **110**, 76-82 (2015).

[24] L. Vina, S. Logothetidis, and M. Cardona, Temperature dependence of the dielectric function of germanium, *Phys. Rev. B* **30**, 1979-1991 (1984).

[25] V. R. D'costa, C. S. Cook, A. G. Birdwell, C. L. Littler, M. Canonico, S. Zollner, J. Kouvetakis, J. Menéndez, Optical critical points of thin-film $Ge_{1-y}Sn_y$ alloys: a comparative $Ge_{1-y}Sn_y/Ge_{1-x}Si_x$ study, *Phys. Rev.* B **73**, 125207 (2006).

[26] C. J. Vineis, Complex dielectric function of biaxial tensile strained silicon by spectroscopic ellipsometry, *Physical Review* B **71**, 245205, (2005).

[27] R. People and J. C. Bean, Calculation of critical layer thickness versus lattice mismatch for Ge_xSi_{1-x}/Si strained-layer heterostructures, *Appl. Phys. Lett.* **47**, 322-324 (1985).

[28] J. Liu, X. Sun, D. Pan, X. Wang, L. C. Kimerling, T. L. Koch, J. Michel, Tensile-strained, n-type Ge as a gain medium for monolithic laser integration on Si, *Optics Express* **15**, 11272-11277 (2007).

[29] S. Assali, A. Attiaoui, P. D. Vecchio, S. Mukherjee, J. Nicolas, O. Moutanabbir, A Light-Hole Germanium Quantum Well on Silicon, *Adv. Mater.* **34**, 2201192 (2022).

[30] S. Lischke, A. Peczek, J. S. Morgan, K. Sun, D. Steckler, Y. Yamamoto, F. Korndörfer, C. Mai, S. Marschmeyer, M. Fraschke, Ultra-fast germanium photodiode with 3-dB bandwidth of 265 GHz, *Nat. Photon.* **15**, 925–931 (2021).

[31] H. Cotal, C. Fetzer, J. Boisvert, G. Kinsey, R. King, P. Hebert, H. Yoon, N. Karam, III–V multijunction solar cells for concentrating photovoltaics, *Energy Environ. Sci.*, **2**, 174-192 (2009).

[32] M. B. Clavel, F. Murphy-Armando, Y. Xie, K. T. Henry, M. Kuhn, R. J. Bodnar, G. A. Khodaparast, D. Smirnov, J. J. Heremans, M. K. Hudait, Multivalley electron conduction at the indirect-direct crossover point in highly tensile-strained germanium. *Phys. Rev. Appl.* **18**, 064083 (2022).

[33] M. B. Clavel and M. K. Hudait, Band Offset Enhancement of a-Al2O3/Tensile-Ge for High Mobility Nanoscale pMOS Devices, *IEEE Electron Dev. Lett.*, 38, 9, 1196-1199, (Sept. 2017).

[34] M. Clavel, D. Saladukha, P. S. Goley, T. J. Ochalski, F. Murphy-Armando, R. J. Bodnar, M. K. Hudait, Heterogeneously-Grown Tunable Tensile Strained Germanium on Silicon for Photonic Devices, *ACS Appl. Mater. Inter.* **7**, 26470-26481 (2015).

[35] Y. Cordier, J. M. Chauveau, D. Ferre, and J. Dipersio, Comparison of $In_{0.33}Al_{0.67}As/In_{0.34}Ga_{0.66}As$ on GaAs metamorphic high electron mobility transistors grown by molecular beam epitaxy with normal and inverse step on linear graded buffer layers, *J. Vac. Sci. Technol. B* ***18***, 2513-2517, (2000).

[36] J. A. Woollam, B. D. Johs, C. M. Herzinger, J. N. Hilfiker, R. A. Synowicki, C. L. Bungay, Overview of variable-angle spectroscopic ellipsometry (VASE): I. Basic theory and typical applications. *Optical Metrology: A Critical Review* **10294**, 3-28, SPIE (1999).

[37] Guide to Using WVASE: Spectroscopic Ellipsometry Data Acquisition and Analysis Software: Lincoln JA Woollam - NE, USA, 2012

[38] B. Johs, C. M. Herzinger, J. H. Dinan, A. Cornfeld, and J. D. Benson, Development of a parametric optical constant model for $Hg_{1-x}Cd_xTe$ for control of composition by spectroscopic ellipsometry during MBE growth, *Thin Solid Films* **313**, 137-142, (1998).

[39] J. Tauc, R. Grigorovici, A. and Vancu, Optical properties and electronic structure of amorphous germanium, Physica Status Solidi (b) **15**, 627-637 (1966).

[40] P. Liu, P. Longo, A. Zaslavsky, and D. Pacifici, Optical bandgap of single-and multi-layered amorphous germanium ultra-thin films, *J. Appl. Phys*. **119**, 014304 (2016).

[41] A. R. Zanatta, Revisiting the optical bandgap of semiconductors and the proposal of a unified methodology to its determination, *Scientific Reports* **9**, 11225 (2019).

[42] M. Chandrasekhar and F. H. Pollak, Effects of uniaxial stress on the electro-reflectance spectrum of Ge and GaAs, *Phys. Rev.* B **15**, 2127-2144 (1977).

[43] S. Zollner, Optical properties and band structure of unstrained and strained $Si_{1-x}Ge_x$ and $Si_{1-x-y}Ge_xC_y$ alloys, Chapter 12 in *Silicon-Germanium Carbon Alloys, Growth Properties and Applications*, Vol. 15, Edited by S. T. Pantellides and S. Zollner (Taylor and Francis, New York, 2002), pp. 387-444.